

# Numerical Simulation of Sub cooled Boiling Flow in Vertical and in Inclined Pipes.

Mohamed A.Elhelw \*,Mohamed A.Teamah \*\*,Osama A.Elmasri \*\*  
and Mohamed A.Elnakeeb \*\*\*

**Keywords:** Wall heat flux partitioning RPI Model,  
Pipe inclination, Sub cooled Boiling.

## ABSTRACT

The primary goal of this work is to thoroughly examine the sub cooled boiling phenomena in inclined and vertical pipes. The continuity, momentum, and energy equations for each phase serve as the foundation for the mathematical model. For the conditions of critical heat flux connected to Eulerian two fluid model, the modified RPI model was employed. With the aid of CFD software, ANSYS FLUENT R2021, the mathematical model was resolved. The findings, which include axial profiles of the vapor volume fraction and liquid temperature, are in good agreement with the experimental data. As a result of the sharp variations in density, the effects of orientations on heat dissipation have been investigated. Using water as a working fluid at high pressure in flow boiling for vertical, inclined 45°, and horizontal orientations, the volume fraction, liquid temperature, heat transfer coefficient, and pressure drop are examined. The distribution of vapor volume fraction in the pipe, which affects wall temperature are more significantly impacted by the pipe inclination angle. In cases of horizontal and 45° angled flow, the distribution of vapor volume is asymmetric, whereas in vertical orientation, they are symmetric. Additionally, as the inclination angle is decreased, the top wall line's and bottom wall line's temperature gradients rise, reaching its maximum in the horizontal direction.

*Paper Received June, 2024. Revised August, 2024, Accepted September, 2024, Author for Correspondence: Mohamed A. Elhelw \* PhD Student, Mechanical Engineering Department, Faculty of Engineering, Alexandria University, Alexandria – Egypt 21544, ROC.*

*\*\* Professor, Mechanical Engineering Department, Faculty of Engineering, Alexandria University, Alexandria – Egypt 21544, ROC.*

*\*\*\* Professor Assistant, Mechanical Engineering Department, Faculty of Engineering, Alexandria University, Alexandria – Egypt 21544, ROC.*

*– Egypt 21913, ROC.Pingtung, Taiwan 91207, ROC.*

## INTRODUCTION

Flow boiling is used as a heat transfer mechanism in modern practical applications because The orientation of the flow lines at different of its substantial convective heat transfer.inclination angles is caused by natural barriers in the path of the flow lines, which is why inclined pipes are often employed in industrial boilers to create compact size boilers. Because sub-cooled boiling heat transfer in pipes may capture high heat flux with a relatively low wall superheat, it performs better than any other sort of heat transfer process. Furthermore, nuclear power engineering frequently deals with sub-cooled boiling flow in the presence of high mass and heat fluxes. The emergence of bubbles starting as a sign of sub cooled boiling is coming from the heater surface while the bulk temperature is still below saturation. Numerous prior experimental investigations have proven that sub cooled boiling performs better in terms of critical heat flux (CHF) and heat transfer efficiency when compared to saturated boiling. In recent years, different studies of sub-cooled vertical and inclined boiling of water in pipes have been carried out. Extremely few studies using experiments focused on studying the high-pressure sub cooled boiling in a vertical and inclined pipe are available in the literature. Bartolemei and Chanturiya and Bartolomei et al.'s high-pressure axial void fraction data for upward pipe flow can be used as traditional examples. Similar work was also done by Garnier et al. with refrigerant R-12 at moderate pressure. Because of its importance to the nuclear industry, annular be improved. Kefer et al. employed tubes with inner diameters of 12.5 and 24.3 mm at 0°, 45°, 30°, and 90°. For a Froude number greater than 10, they proposed that the orientation of the tube has no effect on the boiling crisis. Shah employed 30 fluids for both horizontal and vertical orientations in both small and regular tubes. He suggested that stratification begins for a Froude number less than 0.04 and that orientation is effective. He recommended further investigation into how orientations are impacted by the Froude number. For a Froude number higher than 0.04, Kandlikar proposed that orientation is ineffective. Particularly gravitational forces cannot be entirely ignored at low mass flow rates. With water serving as the work fluid,

the effect of gravity on boiling flow at atmospheric pressure is anticipated to be insignificant for hydraulic diameters no greater than 2.5 mm, which is less than the 11.7 mm tube diameter used in the testing.

There aren't many modeling studies done for sub-cooled boiling in inclined pipes. as the literature study shows. As a result, a numerical study is carried out to examine the characteristics of flow and heat transfer of boiling subcooled water in vertical and inclined pipes. Comprehensive examination of sub cooled flow boiling and the impact of altering the inclination angle through the application of CFD methodology, juxtaposed with the traditional experimental findings of Bartolomei and Chanturiya. Phase distribution and liquid temperature are examined in relation to pipe slope changes.

### Numerical Model

#### Physical model and computational domain.

The physical model for the current work is shown in Fig. 1 and is a 2 m heated stainless-steel pipe with an outer diameter of 25 mm and an inner diameter of 15.4 mm, with a pipe thickness of 5 mm. This pipe is the same as the experimental one that Bartolomei and Chanturiya studied. The working fluid is water, with a mass flow rate of 900 kg/s.m<sup>2</sup>. Water that has undergone sub cooling to a temperature of 60 K enters the channel at the bottom and rises against gravity. At the pipe wall, the system experiences a constant heat flux of 570 kW/m<sup>2</sup>, and 4.5 MPa saturation pressures are applied. The vapor phase's thermo physical properties are supposed to be at saturation temperature, whereas the liquid phase's properties are modeled as a function of temperature in this study.

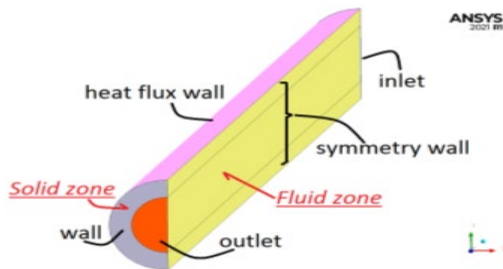


Fig 1. Physical domain with boundary conditions.

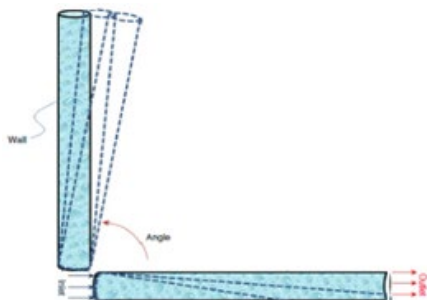


Fig 2. Different Pipe orientation.

A tri-dimensional geometry was selected to ef-

fectively depict the issue in spite of the simulation's high computational cost and convergence requirements. Because of the model's asymmetrical geometry under horizontal and inclined orientations, three-dimensional model is required.

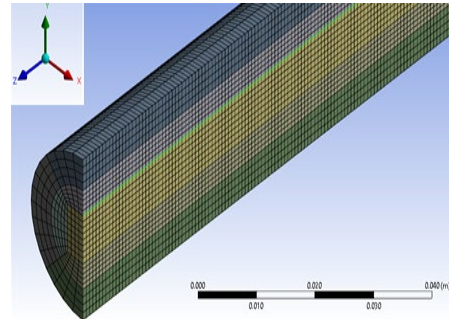


Fig 3. Computational mesh

#### Numerical Model Assumptions and Boundary Conditions.

The computational model of steady-state has been applied. There is a free slip boundary condition for the vapor phase and a no-slip boundary condition for the liquid phase. A pressure boundary condition has been implemented on the heated wall, and a constant heat flux boundary condition has been chosen. At the pipe's inlet, uniform temperature and velocity profiles have been established. Because of the significance of the lift and drag applied to bodies, as well as the transfer of heat and mass across boundaries, it is imperative to establish the proper boundary conditions. Especially in the context of evaporation and condensation, which take place in continuous vapor and liquid phases. The temperature was set to 474.15 K and the Inlet conditions were assigned a velocity of 1.04 m/s. At the outlet, the backflow temperature was adjusted to 530.15 K and a pressure outlet was designated. At the wall boundary, specifically, 0.57 MW/m<sup>2</sup> of heat flux was selected. The turbulence model chosen for the continuous phase is the SST k- $\omega$  model, while the dispersed vapor phase remains laminar. To calculate the bubble-induced turbulence viscosity, the Sato's eddy viscosity model is used.

#### Governing Equations.

Heat transfer correlations and source terms are added to the conservation equations of the Eulerian Multiphase Model (EMM) in the proposed CFD modeling. Using the EMM approach, the conservation equations are formulated for every phase.

The following is an overview of the primary equations for a generic phase.

The volume of phase  $q$ ,  $V_q$ , is defined as

$$V_q = \int_V \alpha_q dV \tag{1}$$

Wherein a system with two phases,

$$\alpha_q + \alpha_p = 1 \tag{2}$$

For phase  $q$ , the mass conservation equation is

provided by

$$\frac{\partial}{\partial t}(\alpha_q \rho_q) + \nabla \cdot (\alpha_q \rho_q \vec{v}_q) = \dot{m}_{pq} - \dot{m}_{qp} \quad (3)$$

where  $\vec{v}_q$  and  $\rho_q$  are the velocity vector and density of phase  $q$ , respectively. The term  $\dot{m}_{pq}$  consists in the mass transfer rate per volume from phase  $p$  to  $q$ , whereas  $\dot{m}_{qp}$  consists in the mass transfer rate per volume from phases  $q$  to  $p$ .

The variable denotes the vapor formation rate per unit of volume, which can be defined as the sum of the interfacial and wall-vapor mass transfer rates. Thus,  $\dot{m}_{lv}$  is comparable to  $\dot{m}_{pq}$  as

$$\dot{m}_{pq} = \dot{m}_{lv} \frac{(T_l - T_{sat})H_{ht}A_i}{L + c_{p,l}(T_{sat} - T_l)} + \frac{\dot{q}_e A_{cell}}{L + c_{p,l}(T_{sat} - T_l)} \quad (4)$$

Here  $A_i$  is the density of the interfacial area,  $A_{cell}$  is the area of the cell face,  $T_l$  is the temperature of the liquid,  $T_{sat}$  is the temperature of saturation,  $L$  is the specific latent heat,  $\dot{q}_e$  is the evaporative heat flux,  $c_{p,l}$  is specific heat of the liquid. The interfacial heat transfer coefficient  $H_{ht}$  is computed using the groundbreaking experimental research of Ranz-Marshall, which developed the following correlation by using the evaporation of spherical water droplets in an upward flow of dry air.

$$H_{ht} = C_{ht} \left[ \frac{k_l}{D_b} (2 + 0.6Re_b^{0.5} Pr^{0.33}) \right] \quad (5)$$

and

$$A_i = \frac{6\alpha_q}{D_b} \quad (6)$$

Whereas the interfacial area density  $A_i$  is given considering equal-size spherical bubbles,  $Re_b$  is the relative Reynolds number based on the diameter of phase  $q$  and the relative velocity  $|\vec{v}_q - \vec{v}_p|$ , and the Prandtl number  $Pr$  is calculated for phase  $p$ . The factor  $C_{ht}$  is the heat transfer coefficient that is adjusted using the heat transfer factor  $H_{ht}$  and is by default set to 1.0. By using the Tolubinsky and Kostanchuk correlation, which states that the bubble diameter of water  $D_b$  is a function of the bulk sub cooling, one can determine the bubble departure diameter.

$$D_b = \min \left( 0.0006 \cdot e^{\frac{\Delta T_{sub}}{45}}, 0.0014 \right) \quad (7)$$

where  $\Delta T_{sub}$  is the degree of sub cooling. For phase  $q$ , the momentum conservation equation yields

$$\frac{\partial}{\partial t}(\alpha_q \rho_q \vec{v}_q) + \nabla \cdot (\alpha_q \rho_q \vec{v}_q \vec{v}_q) = -\alpha_q \nabla P + \nabla \cdot \bar{\tau}_q + \alpha_q \rho_q \vec{g} + \dot{m}_{pq} \vec{v}_p - \dot{m}_{qp} \vec{v}_q + (\vec{F}_{drag,q} + \vec{F}_{lift,q} + \vec{F}_{wl,q} + \vec{F}_{td,q} + \vec{F}_{vm,q}) \quad (8)$$

where  $P$  is the pressure shared by all phases,  $\bar{\tau}_q$  is

the  $q$  phase stress-strain tensor and  $\vec{v}_{pq}$  is the inter-phase velocity. Variables  $\vec{F}_{drag,q}$ ,  $\vec{F}_{lift,q}$ ,  $\vec{F}_{wl,q}$ ,  $\vec{F}_{td,q}$  and  $\vec{F}_{vm,q}$  are the drag force, lift force, wall lubrication force, turbulent dispersion force and virtual mass force, respectively. An interfacial momentum transfer mechanism is connected to each of these forces. The drag force between surfaces per unit of volume. The interfacial drag force per unit of volume  $\vec{F}_{drag,q}$  is calculated as

$$\vec{F}_{drag,q} = K_{pq}(\vec{v}_p - \vec{v}_q) \quad (9)$$

Whereas for liquid-liquid, bubbly, and gas-liquid mixtures, the coefficient of exchange  $K_{pq}$  is typically applied. One way to express the coefficient of exchange is as a function of the particle's relaxation time  $\tau_p$  and drag factor  $f$  as

$$K_{pq} = \frac{\alpha_q \alpha_p \rho_p f}{\tau_p} \quad (10)$$

with

$$\tau_p = \frac{\rho_p D_b^2}{\mu_q} \quad (11)$$

and

$$f = \frac{C_{drag} Re}{24} \quad (12)$$

Schiller and Naumann proposed that the drag factor  $f$  be obtained based on the relative Reynolds number  $Re$ , and that the drag coefficient  $C_{drag}$  for bubbly flows be calculated based on the Ishii and Zuber correlation.

$$C_{drag} = \begin{cases} 24(1 + 0.1Re^{0.687})/Re & Re \leq 1000 \\ 0.44 & Re \geq 1000 \end{cases} \quad (13)$$

The bubble and the liquid phase's shear stress profile interact to produce the lift force. One way to present the general expression is

$$\vec{F}_{lift,q} = -C_{lift} \rho_q \alpha_p (\vec{v}_q - \vec{v}_p) \times (\nabla \times \vec{v}_q) \quad (14)$$

wherein the lift coefficient is determined using the model for couette flows developed by Tomiyama et al., where the lift coefficient  $C_{lift}$  is expressed as a function of the bubble size.

As the force that pushes the bubbles away from the wall and into the liquid bulk, the wall lubrication force  $\vec{F}_{wl,q}$  is described as

$$\vec{F}_{wl,q} = C_{wl} \rho_q \alpha_p |\vec{v}_q - \vec{v}_p|^2 \vec{n}_w \quad (15)$$

Here is the wall lubricant coefficient  $C_{wl}$ , which was calculated for laminar and fully-developed bubbly flow at an adiabatic air-water flow and  $\vec{n}_w$  is the unit vector perpendicular to the wall using the methods of Antal et al.; Lopez-de-Bertodano and Prabhudharwadkar noted that the Antal et al. presented better prediction results than the parameters proposed

by Krepper and Prasser When whirls in the cap bubbly flow cause small bubbles to diffuse, this is represented by the turbulent dispersion force  $\vec{F}_{td,q}$ . According to Lopez-de-Bertodano, this force can be represented in light of

$$\vec{F}_{td,q} = C_{td}\rho_q k_q \nabla \alpha_p \quad (16)$$

While the turbulent dispersion coefficient is represented by and set to 1.0, the turbulent kinetic energy is represented by the variable  $k_q$ . Better agreements with the experimental data have been achieved when the turbulent dispersion coefficient is higher than 0.25, which was initially obtained for adiabatic air-water flows, according to Lopez-de-Bertodano and Prabhudharwadkar. The relative acceleration between phases creates the virtual mass force, which can be explained as follows.

$$\vec{F}_{vm,q} = 0.5\rho_q\alpha_p\left(\frac{d_q\vec{v}_q}{dt} - \frac{d_q\vec{v}_p}{dt}\right) \quad (17)$$

where the term  $\frac{d_q}{dt}$  The phase material time derivative is represented by

$$\frac{d_q\varphi}{dt} = \frac{\partial\varphi}{\partial t} + (\vec{v}_q \cdot \nabla)\varphi \quad (18)$$

For phase  $q$ , the energy conservation equation is provided .

$$\frac{\partial}{\partial t}(\alpha_q\rho_q h_q) + \nabla \cdot (\alpha_q\rho_q \vec{v}_q h_q) = -\alpha_q \frac{\partial p}{\partial t} - \nabla \cdot \vec{q}_q + q_{pq} + (\dot{m}_{pq}h_p - \dot{m}_{qp}h_q) \quad (19)$$

where is the energy exchange term  $q_{pq}$  between the different phases, is the heat flux vector  $\vec{q}_q$ , and the specific enthalpy  $h$ .

This work used the RPI model, a mechanistic approach created by Kurul and Podowski as the boiling model. This method idealizes the boiling phenomenon into average effects that occur over time and space, like bubble nucleation, growth, frequency of departure, and waiting time. The impact of sliding and coalescing bubbles on wall heat transfer is not included in the RPI model, in contrast to the models of Basu et al. and Gilman and Baglietto.

Mechanistic models such as the RPI model provide a way to optimize the use of the local data made available by CFD approaches. Furthermore, the accurate measurement of near wall quantities is crucial for the CFD implementation of the RPI model, as it requires reinterpreting bulk parameter inputs in terms of these quantities. According to a comprehensive search of the public literature, there is a dearth of this data, which hinders the development of these sub-models. It would be beneficial to conduct more targeted experimental measurements.

The entire heat flux from a wall to a liquid is divided into three parts by the RPI model as

$$\dot{q}_w = \dot{q}_l + \dot{q}_q + \dot{q}_e \quad (20)$$

where  $\dot{q}_l$ ,  $\dot{q}_q$  and  $\dot{q}_e$  are heat fluxes associated with

liquid convection, quenching, and evaporation, respectively, and. The wall is separated into two portions under bubbly two-phase flow: portion  $\phi$  ( $0 \leq \phi \leq 1$ ), which is covered in nucleating bubbles, and portion  $(1 - \phi)$ , which is covered in fluid. Additionally, heat is transferred to the liquid phase outside of the bubbles' influence zone, characterizing the convective heat flux  $\dot{q}_l$ , which is expressed as

$$\dot{q}_l = H_l(T_w - T_l^{cell})(1 - \phi) \quad (21)$$

This is the liquid phase's single-phase heat transfer coefficient  $H_l$ , which was calculated based on the flow regime. The following expression can be used to define the area of influence  $\phi$  based on the bubble departure diameter and nucleate site density:

$$\phi = \min\left(1, C_\phi N_w D_b^2 \frac{\pi}{4}\right) \quad (22)$$

The Del Valle and Kenning correlation provides an empirical method for obtaining the area of influence coefficient  $C_\phi$ , which is described as

$$C_\phi = 4.8e^{\left(\frac{Ja}{80}\right)} \quad (23)$$

Where  $Ja$  is the sub cooled Jacob number, which can be found by using

$$Ja = \frac{\rho_l c_{p,l} \Delta T_{sub}}{\rho_v L} \quad (24)$$

As a function of wall superheat, the nucleate site density is represented by the Lemmert-Chawla correlation. Consequently,

$$N_w = C_N (\Delta T_{sup})^m \quad (25)$$

where by default, as well as. Numerous authors, like Koncar et al., have improved the Lemmert-Chawla correlation by adjusting the constants  $C_N$  and  $m$ .

After the bubble detaches, the liquid fills the wall's vicinity, resulting in additional energy transfer known as the quenching heat flux  $\dot{q}_q$ . It is defined as.

$$\dot{q}_q = 2\pi^{-0.5}\phi(C_q f_b \kappa_l \rho_l c_{p,l})^{0.5} (T_w - T_l^{cell}) \quad (26)$$

The bubble departure frequency  $f_b$  is the variable, while the thermal conductivity, density, and specific heat of the liquid phase are  $\kappa_l$ ,  $\rho_l$  and  $c_{p,l}$ , in that order, and. The factor, which has a default value of 1.0, is the quenching factor  $C_q$  used to control the bubble departure frequency. Cole's proposal of inertia controlled growth serves as the basis for the calculation of the bubble departure frequency. Consequently,

$$f_b = \left[ \frac{4g(\rho_l - \rho_v)}{3\rho_l D_b} \right]^{-0.5} \quad (27)$$

The force balance of a bubble rising upward at terminal velocity in a liquid pool was used to derive this expression. This condition has been used as the standard correlation for the prediction of the departure fre-

quency under pool and flow boiling conditions, despite having little relationship to the expected frequency at low qualities under forced convection. The net heat to form the vapor phase, or evaporative heat flux, is given by

$$\dot{q}_e = \frac{\pi}{6} D_b^3 f_b N_w \rho_v L \quad (28)$$

The mathematical model could take into account a number of additional interaction sub-models. Li et al. had previously assessed and suggested the sub-models used in this study for the prediction of boiling and critical heat flux.

All simulation cases used the mixture turbulence model, which is the multiphase turbulence model that ANSYS FLUENT 2021 R1 defaults to. In this instance, the key elements of the turbulent flow are satisfactorily captured by the combination of mixture properties and mixture velocity. The SST  $k - \omega$  model was selected as the turbulence model, as recommended by Li et al. While the wall treatment approach of all other turbulence models is chosen in advance and might not be appropriate for the flow development along the channel, the wall estimate method for SST  $k - \omega$  model is scaled with near-wall grids.

Transport equations for the SST  $k - \omega$  model are given by:

$$\frac{\partial}{\partial t}(\rho k) + \frac{\partial}{\partial x_i}(\rho k u_i) = \frac{\partial}{\partial x_j}(\Gamma_k \frac{\partial}{\partial x_j}) + \tilde{G}_k - Y_k + S_k \quad (29)$$

$$\frac{\partial}{\partial t}(\rho \omega) + \frac{\partial}{\partial x_i}(\rho \omega u_i) = \frac{\partial}{\partial x_j}(\Gamma_\omega \frac{\partial}{\partial x_j}) + G_\omega - Y_\omega + D_\omega + S_\omega \quad (30)$$

In these equations  $\tilde{G}_k$  represents the generation of turbulence kinetic energy due to mean velocity gradients  $G_\omega$  represents the generation of  $\omega$ ,  $\Gamma_k$  and  $\Gamma_\omega$  represent the effective diffusivity of  $k$  and  $\omega$ , respectively,  $Y_k$  and  $Y_\omega$  represent the dissipation of  $k$  and  $\omega$  due to turbulence,  $D_\omega$  represents the cross-diffusion term,  $S_k$  and  $S_\omega$  are source terms.

Turbulence kinetic energy  $k$  and specific dissipation rate  $\omega$  are calculated from

$$k = \frac{3}{2} (U_{avg} I)^2 \quad (31)$$

$$\omega = \frac{\frac{1}{k^2}}{C_\mu^{1/4} l} \quad (32)$$

Where,  $U_{avg}$  is the mean flow velocity, turbulence intensity  $I=0.16(Re)^{-1/8}$  turbulence length  $l=0.07L$ .

The constants in SST  $k-\omega$  model are considered as:

$$\sigma_{k,1} = 1.176, \sigma_{\omega,1} = 2.0, \sigma_{k,2} = 1.0, \sigma_{\omega,2} = 1.168, \alpha_1 = 0.31, \beta_{i,1} = 0.075$$

$$\beta_{i,2} = 0.0828, k=0.41, C_\mu = 0.09$$

The SST  $k - \omega$  turbulence model computes more accurate drag coefficient for slender bodies.

### Grid Independence Check.

For the computational domain that has been chosen, a structured mesh pattern is used, at the walls, where the meshes are finer. Different combinations are investigated to guarantee that the solution is independent of the grid. Fig. 4 displays axial volume fraction profiles ( $\alpha_v$ ) for four distinct mesh structures during the vapor phase. Meshes with 88 K, 166 K, 318 K, 455 K, and 512 K volumes were made. The way the vapor volume fraction behaves in relation to vertical location along the channel is almost the same in the results obtained with various meshes. Coarser meshes allow for the achievement of mesh independent solutions. Thus, the mesh with 318K volumes was used for the remaining cases in this study.

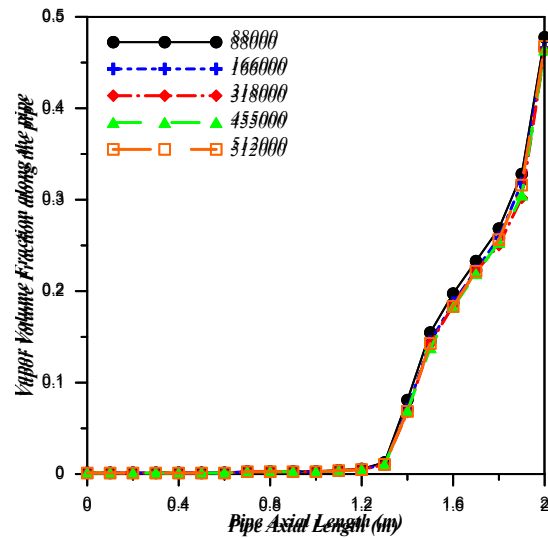


Figure 4. Mesh dependency check (4.5 MPa and 570 kW/m<sup>2</sup>).

### Validation of the numerical method.

In this study, two distinct benchmark test cases with different geometries were simulated. As a result, by contrasting the numerical results with the two sets of experimental data of references, each set was independently validated. Figures 5(a), (b), (c) show the axial variations of vapor volume fraction, liquid temperature, and surface temperature respectively. The current numerical results were compared with experimental data of benchmark test case from Bartolomoj et al. As a result, as seen in Fig. 5(a), the vapor volume fraction also began to rise steadily from  $y = 1.2$  m. There is a good degree of agreement between the current numerical and experimental data, as indicated by the maximum deviation of 14% regarding the experimental data of vapor volume fraction.

Also demonstrating high accuracy of the numerical results in Fig. 5(b) for liquid temperature with maximum deviation percentage of 5%. Furthermore, Fig. 5(c) demonstrates that the surface temperature first rose before changing from liquid to vapor and finally becoming nearly constant with maximum deviation percentage of 7%.

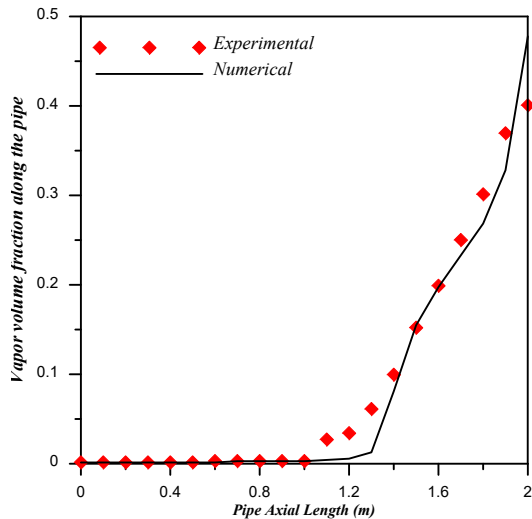


Figure 5a. vapor volume fraction (4.5 MPa and 570 kW/m<sup>2</sup>).

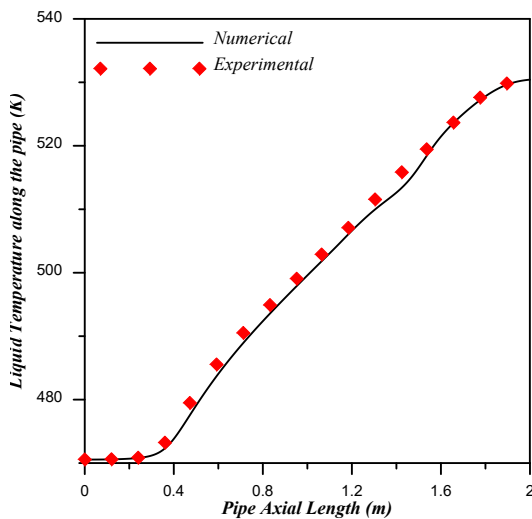


Figure 5b. Liquid temperature along the pipe (4.5 MPa and 570 kW/m<sup>2</sup>).

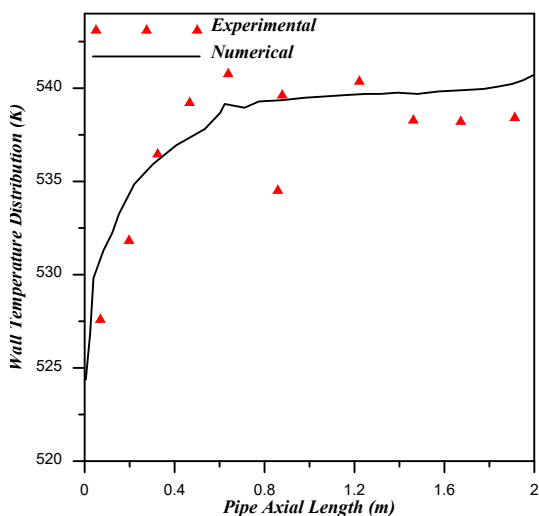


Figure 5c. Wall temperature distribution along the pipe (4.5 MPa and 570 kW/m<sup>2</sup>).

Fig. 6 presents a second comparison of the local sur-

face temperature of current results with experiment of benchmark test case of Hoyer. The surface temperature abruptly increased at  $y = 4$ , which corresponds to the critical heat flux condition, as seen in Fig. 6. In general, the numerical results and the experimental data agreed well. However, the difference increased where  $y > 4$  the dry-out zone. Significant components in the post-dry out heat transfer include the droplet-vapor and steam-wall heat transfers, which determine the surface and vapor temperatures. The surface temperature drop could be caused by the droplets' impact on the pipe's surface. The model's maximum deviation is less than 8%, and its trend aligns with the results of the experiment.

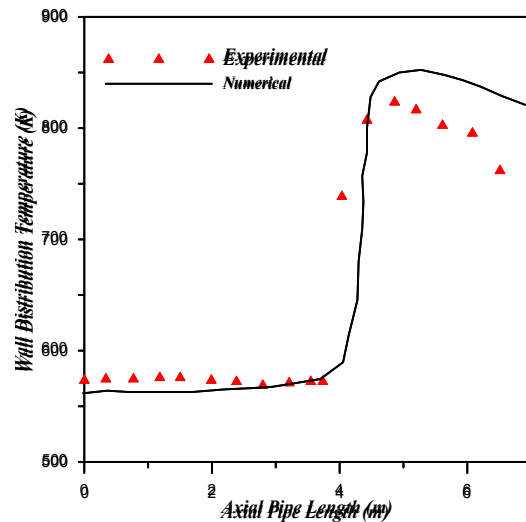


Fig. 6. Numerical and experimental results for axial surface wall temperature .

### Numerical Methodology.

Using a control volume technique, differential equations have been discretized. For the purpose of spatial discretization, the First Order Upwind scheme was applied to all equations. The momentum conservation equations were solved in a coupled scheme without the use of pressure-velocity numerical schemes. All simulation cases were subject to a steady state condition, and the solution was deemed to have converged when the residuals of the equation fell below  $10^{-4}$ .

## Results and Discussion

### Effect of inclination angle on phase distribution profile.

Small bubbles are produced at specific locations in sub cooled flow boiling. The tiny bubbles are scattered throughout the steady liquid flow. These tiny bubbles combine to form bigger bubbles, or slugs, as the vapor quality rises. Gravity has an effect on how these long bubbles move. The vapor volume fraction ( $\alpha_v$ ) contours are displayed in Fig. 7-9 in four sections, each of which depicts a quarter of the pipe (0.5 m). Moving from lower to upper sections, the fluid enters

the bottom section and moves on. A sequence of modifications in the flow regime patterns are typically brought about by the acceleration of the flow, which produces different liquid and vapor velocities. It is evident that at the inlet, only pure liquid enters the pipe, tiny vapor bubbles form on the heated wall, and the bubbles' coalescence and evaporation cause the void fraction to gradually rise. These massive structures eventually coalesce into deformed slugs that rise to the top of the pipe due to upward flow and buoyancy. In the symmetry plane, the contours of the vapor volume fraction ( $\alpha_v$ ) for vertical pipe ( $\beta = 90^\circ$ ) are shown in Fig.7.

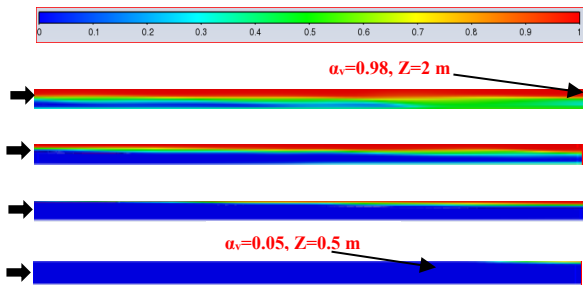


Fig 7. Vapor volume fraction contours along the pipe vertical

When the symmetry plane is oriented vertically, its right line is at rotation angle  $\Theta = 0^\circ$  and its left line is at  $\Theta = 180^\circ$ . As depicted in Fig 7, the thermal system's vapor volume fraction ( $\alpha_v$ ) distribution is symmetric. The centerline of the pipe displays the lowest values, while the neighborhoods surrounding its internal walls exhibit the highest  $\alpha_v$  values. Steam production spreads across a larger portion of the inner wall as the fluid advances. The flow is monophasic and liquid phase in this zone, as indicated by the volume fraction ( $\alpha_v$ ) of 0 at the pipe inlet. A significant section of the transversal area ( $A_{tr} = 70\%$ ) is occupied by vapor at the pipe outlet; the average value of  $\alpha_v = 0.41$  and the maximum value of  $\alpha_v$  is 0.62, are found in  $R = 7.7$  mm. It was discovered that the symmetric distribution of vapor in the pipe disappears for inclined  $45^\circ$  and horizontal orientation, and vapor tends to collect on the upper surface. Nearly all of the vapor produced on the lower wall immediately leaves it to join the vapor stream on the top section due to the gravity effect for the horizontal case, which is perpendicular to the flow direction. However, in the inclined  $45^\circ$  case, the liquid stream's temperature rises to reach the phase change state earlier than in the horizontal case due to the gravity component acting in the pipe's axial direction. The contours of  $\alpha_v$  at a  $45^\circ$  inclination angle are shown in Fig. 8. It is observed that vapor generation begins earlier at the top line at  $Z = 0.5$  m and the vapor volume fraction increase along the pipe. The contours of  $\alpha_v$  in the case of horizontal orientation are displayed in Fig. 9. It is noted that at  $Z = 0.4$  m, the top line is where the vapor nucleation along the pipe begins. By contrasting the vapor volume fractions for horizontal, inclined  $45^\circ$ , and vertical cases, it is evident that when the pipe

inclination is changed from vertical to horizontal, the results are consistent. The symmetric pattern of vapor formation is broken, and as a result of changes in applied gravity, the tip of the vapor cone inside the pipe begins to approach the upper wall line. In both the horizontal and inclined  $45^\circ$  orientations, the phasic distribution is asymmetric with respect to the tube's radial direction.

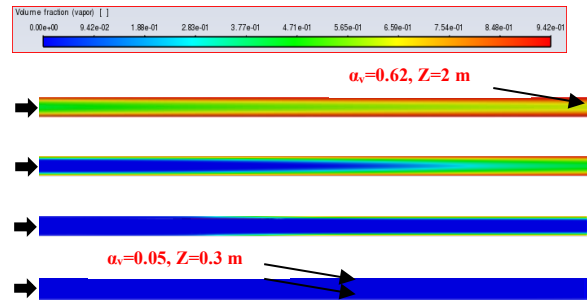


Fig.8 Vapor Volume Fraction Contours along inclined  $45^\circ$  pipe.

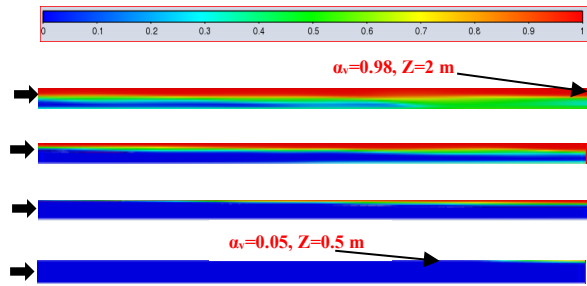


Fig.9 Vapor Volume Fraction Contours along horizontal pipe.

With the intention of making the conditions at the fluid's outlet more apparent, the contour features of Figs. 10a, b, and c are limited to the last centimeter of the pipe. Fig. 10a shows that the maximum values of  $\alpha_v$  are observed close to the wall, reaching 0.7, and that the values decrease to 0.4 as they approach the pipe's center ( $R_i = 0$  m). When the angle is  $45^\circ$ , the vapor nearly fills the transversal outlet area ( $A_{tr} = 50\%$ ), with the maximum  $\alpha_v$  of 0.95 found at the pipe outlet. More than 40% of the pipe at the outlet section is also taken up by the higher void fraction values. Vapor fills more than half of the transversal outlet area ( $A_{tr} = 60\%$ ) in a horizontal pipe; the maximum value of  $\alpha_v$  is 1 at the pipe outlet, where  $r = 7.7$  mm. Additionally, the pipe at the outlet section has more than 50% of its area taken up by the higher void fraction values.

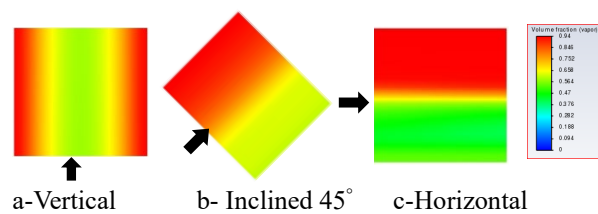


Fig 10. vapor volume fraction contour at the last 0.01 m of pipe.

The average vapor volume fraction ( $\alpha_v$ ) for each of the three cases are compared in Fig 11. After taking an average in the Y direction, the numerical data were obtained, producing 21 points in the Z direction, beginning at Z = 0 m and separated by 0.1 m. The average volume fraction of vapor ( $\alpha_v$ ) profile for an inclined 45° replicates the numerical data from the horizontal case, with the exception of the last 0.6 meters of the pipe, where there is minimal variation in vapor density close to the heated walls. The formation of vapor bubbles in the vertical case occurs later than in the inclined 45° and horizontal cases, but they follow the same profile of horizontal case towards the pipe's end.

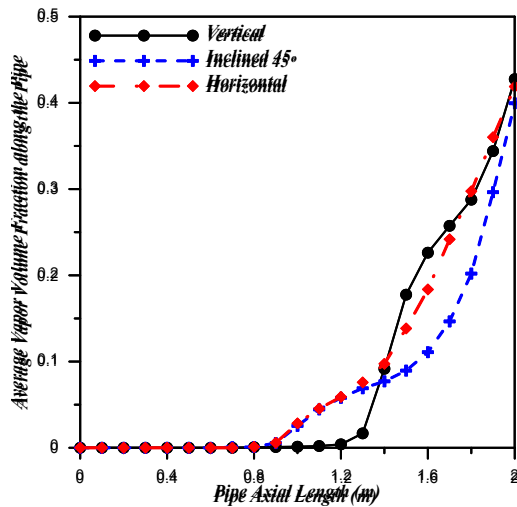


Fig. 11 Vapor volume fraction along the pipe.

The profiles of Average liquid temperature ( $T_L$ ) for the three cases are displayed in Fig. 12. The numerical profiles for the liquid's temperature profile are identical in all three cases.

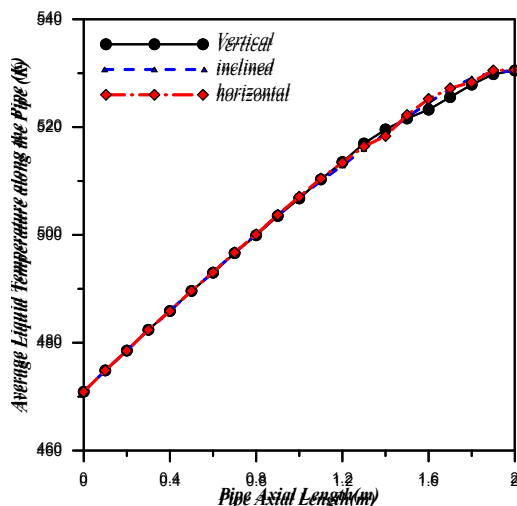


Fig. 12 Average Liquid Temperature along the pipe.

**Effect of inclination on heat transfer coefficient along the pipe.**

The variation in the local heat transfer coefficient along the axial length of the pipe at two different

radial locations around its circumference: the bottom wall line ( $\Theta = 180^\circ$ ) and the top wall line ( $\Theta = 0^\circ$ ). To investigate the quantitative circumferential distribution along the axial direction of the pipe for each of the three orientations, a constant heat input is considered. The profiles of wall heat transfer coefficient ( $h$ ) show that bulk fluid temperature profiles for various inclination angles follow the same trend. The bulk value is determined by integrating the quantity along the same axial plane. The local heat transfer coefficient has been estimated at any axial location as the ratio of wall heat flux and wall to bulk temperature differential. Throughout the single-phase regime, however,  $h$  essentially stays the same. The heat transfer coefficient's slope varies along the pipe's axial length in the sub cooled zone. At the saturation point, the heat transfer coefficient increases and reaches its maximum value. The magnitude decreases significantly at the convective flux disappearance point. Because of the vapor phase's low thermal conductivity, which prevents the liquid from coming into contact with the heated surface, the heat transfer mechanism is significantly weakened, as shown by the profiles. In Fig.13 the direction of the fluid's shear force and the gravitational force coincide in the vertical orientation. As a result, during boiling, the bubbles easily separate from the surface and rise from the pipe's core. As a result, there is little variation in wall temperature along the radial direction. The local heat transfer distribution for the left and right walls is likewise symmetric, reaching its maximum value at Z = 1.3 m. This is because the distribution of vapor bubbles is symmetric about the pipe's radius as well as throughout its circumference. Due to the combined effects of buoyancy and gravity, the vapor bubbles in the pipe flow smoothly. Vapor bubbles are dispersed unevenly in the liquid and close to the heated walls for horizontal and 45° angles. As a result, there is an asymmetric distribution of the heat transfer coefficient. When a pipe is inclined 45°, the local heat transfer distribution varies along its radial length because the bottom wall has a thin layer of liquid and the upper portion of the pipe is filled with vapor in the form of formed bubbles. As the heat transfer coefficient rises, it reaches its maximum for the bottom line at Z=1.9 m and the top line at Z= 0.75 m as shown in Fig 14. The asymmetric distribution of the liquid and vapor phases is visible for horizontal directions due to the gravitational effect. The rapidly moving liquid-bubble slug interface at the top surface causes a sudden change in temperature and heat transfer coefficient, which is where the abrupt heat transfer coefficient distribution is observed in Fig.15. For a given section of the pipe, the accumulation of vapor slug is greater in the horizontal case than the inclined 45° case. This results in higher values for the heat transfer coefficient for both the top and bottom walls at higher axial lengths than in the inclined 45° case. At the pipe's top and bottom walls, the local heat transfer coefficients are almost equal for the first section. For

over 50% of the pipe portions, the asymmetric heat transfer coefficient distribution is covered.

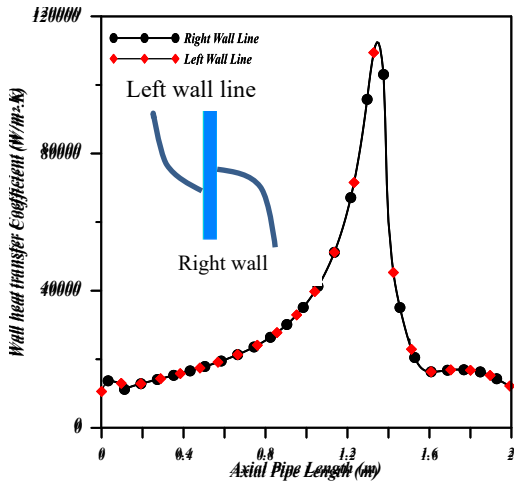


Fig. 13 local heat transfer coefficient for top and bottom wall in Vertical pipe.

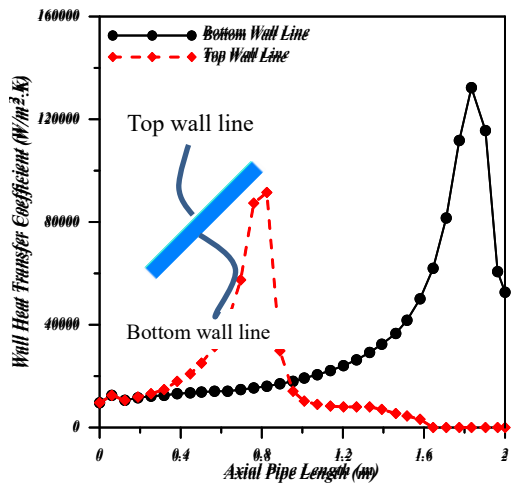


Fig. 14 Local heat transfer coefficient for top and bottom wall in inclined 45° pipe

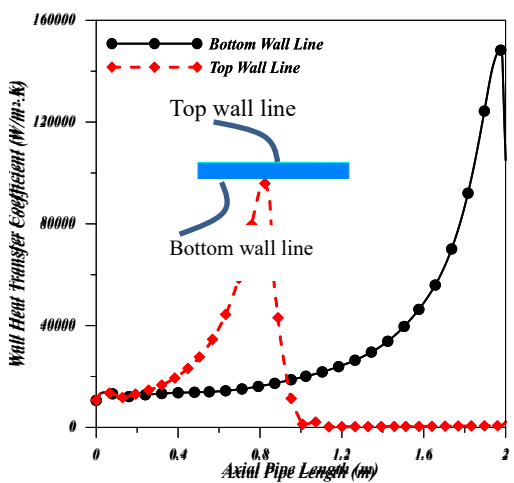


Fig. 15 local heat transfer coefficient for top and bottom wall in horizontal pipe.

**Effect of inclination angle on pressure drop inside the pipe.**

The pressure drop curve along the flow direction is depicted in Fig.16. Because of friction loss, pressure generally decreases linearly with pipe length, with inlet pressure being slightly higher than outlet pressure. There are two primary causes of the pressure drop across the pipe: friction and gravity. As the bulk temperature rises and friction loss occurs, the pressure in the single-phase portion of the pipe decreases slightly. The pressure drop starts to rise again when the inlet bulk temperature reaches a particular point because the wall superheat is now high enough to cause bubbles. Sub cooled boiling occurs throughout the entire pipe as the inlet bulk temperature rises, increasing the pressure drop across the pipe. A notable rise in void fraction causes a sharp increase in pressure drop in the sub cooled boiling region. Since the gravitational term makes up the majority of the pressure drop in a vertical pipe, a sharp increase in the void fraction appears to result in a corresponding decrease in the overall pressure drop.

As the flow boils, the frictional fraction becomes more significant and the overall pressure drop through the pipe rises as a result of the bubbles forming, which increases the roughness of the flow. Because of the change in the direction of gravity, the frictional component of pressure drop dominates in the horizontal case. Because of the variance in bubble density created near the top and bottom lines in the final section of the pipe, the pressure drop profile deviates from a linear format.

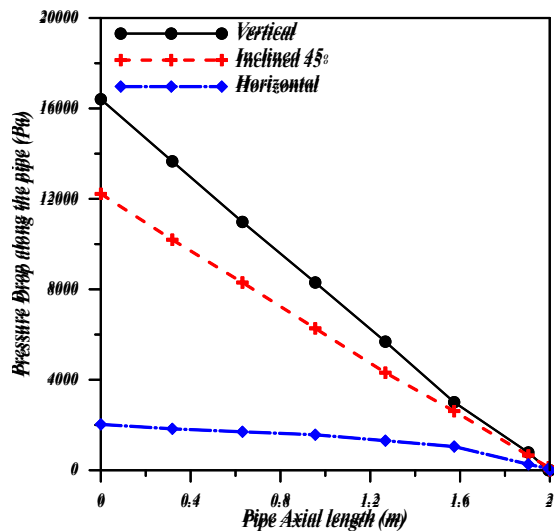


Fig. 16 pressure drop along the Pipe (over  $Ri=0$ ).

**Conclusion**

This article's numerical simulation of the 3D model validates and satisfactorily reproduces the experimental findings presented in the literature. The impact of varying the inclination angle on the boiling flow within the pipe is examined based on the analysis. Evaluations are done on the distribution of vapor phase, liquid temperature, local heat transfer coefficient, and pressure drops inside the pipe. We came at

the following conclusions from the study:

1. The average vapor volume fraction along the pipe agrees well with the experimental results, as calculated numerically. For liquid temperature, the numerical profile replicates the experimental data.
2. The vapor volume fraction distribution inside the pipe, which cause variations in wall temperature, are more significantly impacted by the pipe inclination angle. For inclined 45° and horizontal orientation, the phasic distribution is asymmetric about the pipe's radial direction and symmetric in vertical orientation.
3. The distribution of local heat transfer adjacent to both pipe walls in vertical orientation is symmetric and identical because the distribution of vapor bubbles is symmetric; additionally, maximum values are reached after the middle of the pipe. As the inclination angle decreases, the local heat transfer coefficient distribution becomes asymmetric, and the density of vapor bubbles adjacent to the top wall increases. Denser vapor accumulation near the top wall results in faster and earlier propagation of the heat transfer coefficient than the bottom wall.
4. The shape of the pressure drop profile is nearly identical and linear; however, as the inclination angle is decreased, the pressure drop value across the pipe decreases because of the diminished gravity effect. Because of the shift in gravity, the pressure drop diminishes once more in the horizontal case.

### Future Work

Future studies will perform sensitivity analyses and look into the effects of different operating parameters like mass flux, pressure, heat flux, and inlet subcooling temperature.

### References

- A. Kubilay, D. Derome, B. Blocken, and J. Carmeliet, "CFD simulation and validation of wind-driven rain on a building facade with an Eulerian multiphase model," *Building and environment*, vol. 61, pp. 69-81, 2013.
- A. Tomiyama, H. Tamai, I. Zun, and S. Hosokawa, "Transverse migration of single bubbles in simple shear flows," *Chemical Engineering Science*, vol. 57, no. 11, pp. 1849-1858, 2002.
- B. Končar, I. Kljenak, and B. Mavko, "Modelling of local two-phase flow parameters in upward subcooled flow boiling at low pressure," *International Journal of Heat and Mass Transfer*, vol. 47, no. 6-7, pp. 1499-1513, 2004.
- E. Eskandari, H. Alimoradi, M. Pourbagian, and M. Shams, "Numerical investigation and deep learning-based prediction of heat transfer characteristics and bubble dynamics of subcooled flow boiling in a vertical tube," *Korean Journal of Chemical Engineering*, vol. 39, no. 12, pp. 3227-3245, 2022.
- E. Krepper and H.-M. Prasser, "Measurements and CFX-Simulations of a bubbly flow in a vertical pipe," *WIT Transactions on Engineering Sciences*, vol. 29, 1970.
- G. Bartolomei and V. Chanturiya, "Experimental study of true void fraction when boiling subcooled water in vertical tubes," *Thermal Engineering*, vol. 14, no. 2, pp. 123-128, 1967.
- G. Bartolomei et al., "An experimental investigation of true volumetric vapor content with subcooled boiling in tubes," *Thermal Engineering*, vol. 29, no. 3, pp. 132-135, 1982.
- H. Li, S. A. Vasquez, H. Punekar, and R. Muralikrishnan, "Prediction of boiling and critical heat flux using an eulerian multiphase boiling model," in *ASME International Mechanical Engineering Congress and Exposition*, 2011, vol. 54921, pp. 463-476.
- H. Victor, M. Del Valle, and D. Kenning, "Subcooled flow boiling at high heat flux," *Int. J. Heat Mass Transfer*, vol. 28, no. 10, pp. 1907-1920, 1985.
- J. Straub, "Boiling heat transfer and bubble dynamics in microgravity," in *Advances in Heat Transfer*, vol. 35: Elsevier, 2001, pp. 57-172.
- L. Gilman and E. Baglietto, "Advancements on wall boiling modeling in CFD: leveraging new understanding from MIT flow boiling facility," *NURETH-15, Pisa, Italy*, 2013.
- L. Schiller and A. Naumann, "A drag coefficient correlation. Vdi Zeitung, 77: 318-320, 1935," *Cité page*, vol. 38, 1935.
- M. Ishii and N. Zuber, "Drag coefficient and relative velocity in bubbly, droplet or particulate flows," *AIChE journal*, vol. 25, no. 5, pp. 843-855, 1979.
- M. L. de Bertodano and D. Prabhudharwadkar, "CFD two fluid model for adiabatic and boiling bubbly flows in ducts," in *Computational Fluid Dynamics*: IntechOpen, 2010, p. 29.
- M. Lemmert and J. Chawla, "Influence of flow velocity on surface boiling heat transfer coefficient," *Heat Transfer in Boiling*, vol. 237, no. 247, 1977.
- M. M. Karim, M. Rahman, and M. A. Alim, "Performance of SST k- $\omega$  turbulence model for computation of viscous drag of axisymmetric underwater bodies," 2011.
- M. M. Shah, "Unified correlation for heat transfer during boiling in plain mini/micro and conventional channels," *international journal of refrigeration*, vol. 74, pp. 606-626, 2017.
- N. Basu, G. R. Warriar, and V. K. Dhir, "Wall heat flux partitioning during subcooled flow boiling: Part 1—model development," *J. Heat Transfer*, vol. 127, no. 2, pp. 131-140, 2005.
- N. Hoyer, "Calculation of dryout and post-dryout heat

- transfer for tube geometry," *International journal of multiphase flow*, vol. 24, no. 2, pp. 319-334, 1998.
- N.Kurul and M. Z. Podowski, "Multidimensional effects in forced convection subcooled boiling," in *International Heat Transfer Conference Digital Library*, 1990: Begel House Inc.
- P. Griffith, "Multiphase flow in pipes," *Journal of petroleum technology*, vol. 36, no. 03, pp. 361-367, 1984.
- R. Cole, "A photographic study of pool boiling in the region of the critical heat flux," *AIChE Journal*, vol. 6, no. 4, pp. 533-538, 1960.
- R. D. Boyd, "Subcooled flow boiling critical heat flux (CHF) and its application to fusion energy components. Part I. A review of fundamentals of CHF and related data base," *Fusion Technology*, vol. 7, no. 1, pp. 7-30, 1985.
- R. Kamatchi and S. Venkatachalapathy, "Parametric study of pool boiling heat transfer with nanofluids for the enhancement of critical heat flux: a review," *International Journal of Thermal Sciences*, vol. 87, pp. 228-240, 2015.
- R.Lahey Jr, *Boiling heat transfer: modern developments and advances*. Elsevier, 2013.
- S. Antal, R. Lahey Jr, and J. Flaherty, "Analysis of phase distribution in fully developed laminar bubbly two-phase flow," *International journal of multiphase flow*, vol. 17, no. 5, pp. 635-652, 1991.
- S. G. Kandlikar, "A general correlation for saturated two-phase flow boiling heat transfer inside horizontal and vertical tubes," 1990.
- V. Kefer, W. Kähler, and W. Kastner, "Critical heat flux (CHF) and post-CHF heat transfer in horizontal and inclined evaporator tubes," *International journal of multiphase flow*, vol. 15, no. 3, pp. 385-392, 1989.
- V. Tolubinsky and D. Kostanchuk, "Vapour bubbles growth rate and heat transfer intensity at subcooled water boiling," in *International Heat Transfer Conference 4*, 1970, vol. 23: Begel House Inc.
- W. E. Ranz, "Evaporation from Drops-I and-II," *Chem. Eng. Progr.*, vol. 48, pp. 141-146,173-180, 1952.
- W. Wang, S. Huang, and X. Luo, "MD simulation on nano-scale heat transfer mechanism of sub-cooled boiling on nano-structured surface," *International Journal of Heat and Mass Transfer*, vol. 100, pp. 276-286, 2016.
- X. Zhang, X. Cheng, and W. Liu, "Development of a new semi-mechanistic wall boiling heat transfer model for CFD methodology focusing on macroscopic parameters," *International Journal of Heat and Mass Transfer*, vol. 224, p. 125309, 2024.
- Y. Sato, M. Sadatomi, and K. Sekoguchi, "Momentum and heat transfer in two-phase bubble flow—I. Theory," *International Journal of Multiphase Flow*, vol. 7, no. 2, pp. 167-177, 1981.